Spectrally resolved opacities and Rosseland and Planck mean opacities of lowly ionized gold plasmas: A detailed level-accounting investigation

Jiaolong Zeng and Jianmin Yuan
Department of Physics, National University of Defense Technology, Changsha 410073, People's Republic of China
(Received 22 March 2007; revised manuscript received 11 June 2007; published 7 August 2007)

Calculation details of radiative opacity for lowly ionized gold plasmas by using our developed fully relativistic detailed level-accounting approach are presented to show the importance of accurate atomic data for a quantitative reproduction of the experimental observations. Even though a huge number of transition lines are involved in the radiative absorption of high-Z plasmas so that one believes that statistical models can often give a reasonable description of their opacities, we first show in detail that an adequate treatment of physical effects, in particular the configuration interaction (including the core-valence electron correlation), is essential to produce atomic data of bound-bound and bound-free processes for gold plasmas, which are accurate enough to correctly explain the relative intensity of two strong absorption peaks experimentally observed located near photon energy of 70 and 80 eV. A detailed study is also carried out for gold plasmas of an average ionization degree sequence of 10, for both spectrally resolved opacities and Rosseland and Planck means. For comparison, results obtained by using an average atom model are also given to show that even for a relatively higher density of matter, correlation effects are also important to predict the correct positions of absorption peaks of transition arrays.

DOI: 10.1103/PhysRevE.76.026401 PACS number(s): 52.25.Os

I. INTRODUCTION

Radiative opacity is of great utility in the study of inertial confinement fusion (ICF) [1], stellar physics [2], and x-ray lasers. For the radiative opacity of low-Z plasmas such as aluminum, theoretical results agree well with experiments [3–6]. For mid- and high-Z plasmas, however, there are systematic discrepancies between theory and experiment, which are still unexplained so far [7–9], for both line intensity and position. In order to clarify these discrepancies, combined efforts from both theorist and experimentalist should be made. Experimentally, Iglesias [10] pointed out that unresolved structures in a backlight spectrum can introduce significant errors in the inferred transmission. Theoretically, some physical effects which have been treated approximately or missed in theoretical models may affect the accuracy of opacity. Recently, we [11] gave brief results for the radiative opacity of gold plasmas in the extreme ultraviolet (EUV) energy region by using a detailed level-accounting (DLA) method. It was shown that one has to take into account physical effects such as detailed core-valence electron correlation, line saturation, and relativity adequately to reproduce accurately the experimental observations.

In practical applications, one usually needs radiative opacity in a wide energy range from zero to infinity to determine Rosseland and Planck means. Knowing the radiative opacity only in the EUV energy region is completely insufficient. Therefore, it is necessary and urgent to extend our DLA investigation to the Rosseland and Planck means of gold plasmas. Recently, Jones *et al.* [12] measured the absolute albedos of hohlraums from Au and from high-Z mixtures. Their results showed that the albedo of Au predicted by using the opacity of supertransition arrays (STAs) agrees better with their experimental values than by using that of an average atom (AA) model. It is generally believed that STAs can obtain more accurate opacities than the AA model. Dewald *et al.* [13] carried out the first Au hohlraum experiments at the National Ignition Facility (NIF) using the initial four laser beams to test radiation temperature limits imposed by plasma filling. Radiative opacity, especially Rosseland and Planck mean opacities, play an important role in hydrodynamic simulations to explain experiments.

For Au plasmas, researchers have developed statistical methods such as unresolved transition arrays (UTAs) [14–16], STA [8,17], and AA [18–20] models to calculate the radiative opacity. Recently, Pang *et al.* [21] and Wu *et al.* [22] developed a theoretical approach to calculate radiative opacity of high-Z plasmas including Au plasma in nonlocal thermodynamic equilibrium (non-LTE) by using a detailed configuration-accounting (DCA) approximation. To the best of our knowledge, no other work has been reported in the literature for radiative opacity of Au plasmas by using a DLA method except our recent work [11], although such a model is very important to correctly understand and accurately design relevant experiments. Therefore, it would be helpful and is imperative to study the opacity of high-Z plasmas by using such a detailed approach, with the main physical effects, such as core-valence electron correlation, line saturation, and relativity, being adequately considered.

In addition to the well-reproduced transmission spectra observed by Eidmann *et al.* [8], more details, including changes of positions and strengths of transition lines and changes of photoionization cross sections with different correlations, will be presented in this work. Furthermore, more results of spectrally resolved opacities have been obtained over a wide photon energy range to calculate Rosseland and Planck mean opacities for a variety of plasma conditions of an average ionization degree of 10. These data are not only helpful in analysis of laser-produced plasma experiments but also provide a benchmark for all statistical treatments. In calculations of radiative transfer, one usually needs group opacity. Detailed spectrally resolved opacity data help one to

build a more accurate multigroup model [23]. The effectiveness of the DLA or detailed term-accounting (DTA) approach has been proved for low- and mid-Z plasmas in our previous work [4,24–26].

II. METHOD OF CALCULATION

For a plasma of temperature T and mass density ρ in LTE, radiative opacity at radiation of energy $h\nu$ (h is the Planck constant and ν is the frequency of radiation) is given by

$$\rho\kappa'(h\nu) = [\mu_{bb}(h\nu) + \mu_{bf}(h\nu) + \mu_{ff}(h\nu)](1 - e^{-h\nu/kT}) + \mu_{scatt}(h\nu), \quad (1)$$

where μ_{bb}, μ_{bf}, μ_{ff}, and μ_{scatt} are absorption coefficients contributed by bound-bound, bound-free, free-free, and scattering processes, respectively. The prime on the opacity denotes that stimulated emission has been taken into account.

The bound-bound absorption coefficient can be obtained from the cross sections of bound-bound transition lines:

$$\mu_{bb}(h\nu) = \sum_i \left(\sum_{ll'} N_{il}\sigma_{ill'}(h\nu) \right), \quad (2)$$

where N_{il} is the population of level l for ionization stage i and $\sigma_{ill'}(h\nu)$ is the photoexcitation cross section from level l to l', which can be expressed in terms of the absorption oscillator strength $f_{ill'}$ as

$$\sigma_{ill'}(h\nu) = \frac{\pi he^2}{m_e c} f_{ill'} S(h\nu), \quad (3)$$

where S is the line shape function, which is taken as a Voigt profile, in which linewidths of Doppler and electron impact broadening are included [24].

The contribution of bound-free absorption can be obtained from the photoionization cross sections per ion:

$$\mu_{bf}(h\nu) = \sum_i N_i \sum_l \frac{g_{il} e^{-E_{il}/kT}}{Z_i} \sigma_{il}(h\nu), \quad (4)$$

where N_i is the population of ionization stage i, g_{il} is the statistical weight of level l of ion i, E_{il} is the energy of level l of the ionization stage i above the ground level, k is the Boltzmann constant, and Z_i is the partition function of ionization stage i. The free-free absorption coefficient is obtained from the Kramers cross section, and the scattering contribution is approximated using the Thomson scattering cross section [24].

The populations of different ionization stages, N_i, can be obtained by solving the Saha equation [4,27]

$$\frac{N_{i+1}N_e}{N_i} = \frac{Z_e Z_{i+1}}{Z_i} e^{-(\phi_i - \Delta\phi_i)/kT}, \quad (5)$$

where N_e is the number of free electrons per unit volume, Z_e and Z_i are partition functions of free electrons and ion i, respectively, ϕ_i is the ionization potential (IP) of ionization stage i, and $\Delta\phi_i$ is the depression of the IP caused by the plasma environment restricting the number of bound states available. In this work, we chose the Debye-Huckel model [28] to calculate the IP depression. The population for a given level l of ionization stage i is given by the Boltzmann distribution function.

In practical applications such as radiative transfer, Rosseland and Planck mean opacities are required. They are defined by

$$\frac{1}{K_R} = \int_0^\infty \frac{W_R(u)du}{\kappa'(u)} \quad (6)$$

and

$$K_P = \int_0^\infty [\kappa'(u) - \kappa_{scatt}(u)] W_P(u) du, \quad (7)$$

where $u = h\nu/kT$, $\kappa_{scatt}(u)$ is the opacity contributed by scattering, and W_R and W_P are Rosseland and Planck weighting functions, respectively.

The fraction of radiation transmitted with respect to some incident source of arbitrary intensity is given by

$$F(h\nu) = e^{-\rho\kappa'(h\nu)L}, \quad (8)$$

where L is the path length traversed by the light source through the plasma. To compare directly with experiment, one should include the effects of instrumental broadening, whose mechanism is complicated including, for example, a finite slit width, diffraction effects, and finite resolving power of the instruments. As a general practice, one can integrate theoretical transmission over a Gaussian function, with the full width corresponding to the spectrometer resolution.

III. RESULTS AND DISCUSSION

Eidmann *et al.* [8] measured the transmission spectra of a gold plasma at a density of 0.007 g/cm^3 and temperature of ~20 eV in the photon energy region 40–300 eV. For a gold plasma at a temperature of 22.5 eV and a density of 0.007 g/cm^3, the dominant ionization stages are Au^{8+}-Au^{12+}, accounting for 7.6%, 30.8%, 34.4%, 16.2%, and 9.8%, respectively. To obtain an accurate radiative opacity, one needs accurate atomic data of these ions. In the following, we first analyze the characteristics of the wave function and structure of the relevant ions. Then we discuss the physical effects which influence the accuracy of the calculated atomic energy levels as well as bound-bound and bound-free cross sections. Third, we discuss the combined physical effects on radiative opacity. Finally, spectrally resolved opacities and Rosseland and Planck means are investigated for a sequence of average ionization degree of 10.

A. Characteristics of wave functions and atomic structures

The basic property of atomic structure is determined by wave functions. By analyzing the general features of a wave function, pre-insight into the line strength of optical transitions can be obtained before large-scale calculations are carried out, which always take considerable computer time for heavy material like Au. Therefore, we first show the characteristics of wave functions. Figure 1 shows the radial wave

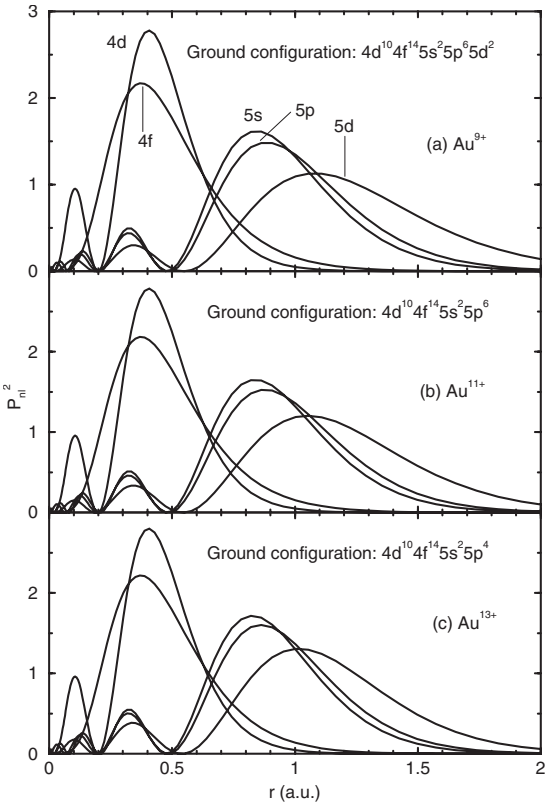

FIG. 1. Radial wave functions of orbitals $4d$, $4f$, $5s$, $5p$, and $5d$ for (a) Au^{9+}, (b) Au^{11+}, and (c) Au^{13+}, respectively.

functions of $4d$, $4f$, $5s$, $5p$, and $5d$ orbitals for Au^{9+}, Au^{11+}, and Au^{13+} ions, respectively. The radial orbitals are obtained from a self-consistent Dirac-Fock-Slater iteration on a fictitious mean configuration with fractional occupation numbers, representing the average electron cloud of the configurations included in the calculations. For different gold ions, the configurations included in the present calculations will be illustrated in the next section. The energy levels of gold ion states are approximated by a linear combination of configuration-state functions, which are constructed from the above-derived radial orbitals. This can be obtained by diagonalizing the relativistic Hamiltonian H (in atomic units):

$$H = \sum_{i}^{N} (c\vec{\alpha} \cdot \vec{\mathbf{p}}_i + (\beta - 1)c^2 + V_{nuc}(r_i) + \sum_{i<j}^{N} \frac{1}{r_{ij}}, \qquad (9)$$

where c is the speed of light in vacuum and $V_{nuc}(r_i)$ is the potential due to the nucleus. Because a fully relativistic treatment is performed for the ionic structure, the large and small components of the relativistic radial orbitals are derived. As the difference of the relativistic radial wave functions of the same orbital angular momentum is very small, we have shown the wave functions of nonrelativistic orbitals in Fig. 1 according to their statistical average.

Note that in order to have a direct comparison among three ions, the same scale of axis for both radius and wave function has been used for all three ions in Fig. 1. Although differences can be seen for three ions (for example, the wave function tends to be inner-wards with an increase of the ionization stage), the wave functions show quite similar features. For all three ions, the wave functions of $5s$ and $5p$ orbitals overlap almost completely. From the positions of nodes of the wave functions, one can also find that cancellation of the radial integral for the optical transition matrix is not considerable. As a result, the optical transition probability (or oscillator strength) between $5s$ and $5p$ orbitals should be very large. For a transition from an initial state Ψ_i to a final state Ψ_j, the length and velocity forms of the weighted oscillator strength is defined by

$$gf_l = \Delta E \left| \left\langle \Psi_i \left| \sum_{p=1}^{N} \vec{\mathbf{r}}_p \right| \Psi_j \right\rangle \right|^2, \qquad (10)$$

$$gf_v = \frac{4}{\Delta E} \left| \left\langle \Psi_i \left| \sum_{p=1}^{N} \nabla_p \right| \Psi_j \right\rangle \right|^2. \qquad (11)$$

where $\Delta E = E_j - E_i$, E_i and E_j are, respectively, the energies of initial and final levels, and g is the statistical weight of the lower level for absorption and of the final state for emission. From the above expression, it is obvious that $|\langle 5s|\Sigma_{p=1}^{N}\vec{\mathbf{r}}_p|5p\rangle|^2$ is very large even though the maximal occupation number of electrons on the $5s$ orbital is only 2.

Similarly, the wave functions of $5p$, $5d$ and $4d$, $4f$ have large overlaps, and as a result, transitions of $5p \rightarrow 5d$ and $4d \rightarrow 4f$ should be very strong as well. Also can be seen that the absorption caused by the former transitions is much stronger than the latter ones. Besides, $4f$ and $5d$ orbitals are also moderately overlapped, and therefore the transitions of $4f \rightarrow 5d$ should also be moderately strong. On the other hand, there are 14 electrons in the $4f$ orbital which contribute to absorption, while there are 6 electrons at most in the $5p$ orbital. From the above analysis, one can expect that the transitions of $5s \rightarrow 5p$, $5p \rightarrow 5d$, $4f \rightarrow 5d$, and $4d \rightarrow 4f$ have dominant contributions to the opacity. Such a conclusion can also be drawn from Fig. 2, which shows the wave functions of the Au^{11+} electron orbitals of (a) $4f$, $5d$, $5g$, $6d$, and $6g$, (b) $5s$, $5p$, and $6p$, and (c) $5p$, $5d$, $6s$, and $6d$. It can easily be seen that the overlaps between $4f$ and $5g$ and between $6d$ and $6g$ are much smaller than that of $4f$ and $5d$. Similarly, the overlaps between $5s$ and $6p$, $5p$, and $6s$, and $5p$ and $6d$ are much smaller than those of $5s$ and $5p$ and $5p$ and $5d$. For higher principal quantum number ($n > 6$), the overlap of wave functions with $4f$, $5s$, and $5p$ orbitals becomes less and less.

Similar characteristics can be found for wave functions of nearby Au ions. Thus the contributions from transitions of $5s \rightarrow 5p$,$5p \rightarrow 5d$, $4f \rightarrow 5d$, and $4d \rightarrow 4f$ to the opacity is much more important than other transitions. As will be demonstrated later, absorption from $5s \rightarrow 5p$, $5p \rightarrow 5d$, and $4f \rightarrow 5d$ transitions is centered at about 85 eV, at which the Rosseland weighting function has its maximal value at the temperature of 22.5 eV. Hence these transitions play the most important role in the Rosseland mean opacity. In the study of opacity, it is intractable to perform a complete configuration interaction (CI) calculation to obtain all necessary bound-bound oscillator strengths, in particular for a heavy

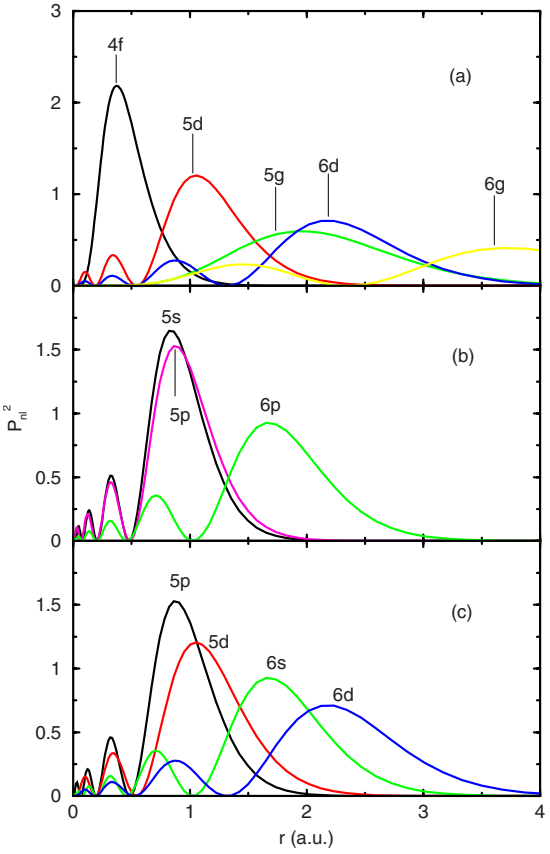

FIG. 2. (Color online) Overlap of radial wave functions of Au^{11+} for transitions of (a) $4f \rightarrow 5d$, $5g$, $6d$ and $6g$, (b) $5s \rightarrow 5p$, $6p$, and (c) $5p \rightarrow 5d$, $6s$ and $6d$, respectively.

material such as Au. However, one can obtain a more accurate opacity by taking the following steps: with a preinvestigation of atomic wave functions, one can carry out a large-scale CI calculation for strong transitions as we discussed above, while for other less dominant absorption, one can obtain the required atomic data using a single Dirac-Fock (DF) calculation which takes the fine-structure levels into account as well.

B. Cross sections of atomic processes

Bound-bound, bound-free, free-free, and scattering processes all contribute to opacity. Among these atomic processes, bound-bound transitions are the most difficult to treat. Below we will discuss the atomic data of bound-bound and bound-free processes.

For the bound-bound absorption process, physical effects such as relativity, CI, nuclear size, the Breit effect, and QED effects will all affect the accuracy of the calculated oscillator strengths. As a result, they should be fully included in a complete treatment. Among these effects, the first two effects are generally the most important ones, though other effects have definite contributions. The oscillator strengths required are obtained by using the flexible atomic code (FAC) developed by Gu [29]. A fully relativistic approach based on the Dirac equation is used throughout the package, and thus relativistic effects have naturally been included. However, the CI effect is a great challenge to theorists for such complex ions. The maximal principal quantum number has commonly been considered to be up to 12 for a gold plasma of about 1% of solid density according to the IP depression. It is not practical to include all CIs in one calculation. To make the calculations tractable, one needs to elaborately choose the configurations. We take Au^{11+} and Au^{10+} as examples to illustrate the scale of CIs included in this work. The ground configuration of Au^{11+} is $([\mathrm{Ni}]4s^24p^6)4d^{10}4f^{14}5s^25p^6$. Electron correlations have been included among the following configurations: $5p^6$, $5p^{-1}nl$, $5s^{-1}nl$, $4f^{-1}nl$, $4d^{-1}nl$, $5p^{-2}nln'l'$, $5s^{-1}5p^{-1}nln'l'$, $4f^{-1}5p^{-1}5dnl$, $4d^{-1}5p^{-1}5dnl$, $5p^{-3}5d^2nl$, $5s^{-1}5p^{-2}5d^2nl$, $4f^{-1}5p^{-2}5d^2nl$, and $4f^{-2}5p^{-1}5d^3$ $(nl,n'l'=5d,5f,5g,6s,6p,6d)$. In the above designation of configurations, full subshells have been omitted for descriptive simplicity. Besides the valence electron correlations, most of the interactions are contributed by core-valence electron correlations, because they are due to excitations of $4d$, $4f$, $5s$, and/or $5p$ core subshells. The oscillator strengths between all levels of these configurations have been obtained in a complete CI calculation. The energetically low levels have been included in these configurations, and they have a dominant contribution to the opacity of plasmas. However, there are many other more transitions from highly excited levels which contribute to opacity. For these line absorptions, we calculate the oscillator strengths for every transition array one by one required for opacity calculation. Using such a mixed method, the oscillator strengths of the transitions between all necessary fine-structure levels have been obtained and the main CI effect on oscillator strengths has been taken into account in bound-bound absorption. The CI effect on oscillator strengths of $5p \rightarrow 5d$ and $4f \rightarrow 5d$ transitions from the ground and first excited configurations $5p^6$ and $5p^55d$ has been demonstrated in our recent work [30].

For Au^{10+} ions, a similar treatment has been used to obtain the required atomic data of bound-bound transitions. Interactions among the following configurations are included: $5p^65d$, $5p^{-1}nln'l'$, $5s^{-1}5dnl$, $4f^{-1}5dnl$, $4d^{-1}5dnl$, $5p^{-2}5d^2nl$, $5s^{-1}5p^{-1}5d^2nl$, $4f^{-1}5p^{-1}5d^2nl$, $5p^{-3}5d^4$, $5p^{-3}5d^35f$, $5p^{-3}5d^36s$, $5s^{-1}5p^{-2}5d^4$, $4f^{-2}5d^3$, $4f^{-2}5d^26s$, and $4f^{-1}5p^{-2}5d^4$ $(nl,n'l'=5d,5f,5g,6s,6p,6d)$. In order to demonstrate the CI effect, Fig. 3 shows the photoabsorption cross sections contributed by transition arrays of $4f^{14}5p^65d \rightarrow 4f^{14}5p^55d^2$ and $4f^{14}5p^65d \rightarrow 4f^{13}5p^65d^2$ by using (a) a single-configuration Dirac-Fock calculation and (b) a large-scale CI calculation. In this figure, lines below 90 eV originate from transitions of $5p \rightarrow 5d$, while lines above 90 eV originate from $4f^{14}5p^65d \rightarrow 4f^{13}5p^65d^2$ transitions. It can easily be seen that the CI effect changes the line intensity distribution considerably. The total oscillator strengths of $5p \rightarrow 5d$ are greatly reduced compared with results of single DF calculations, while those of the $4f \rightarrow 5d$ lines are drastically enhanced. For $5p \rightarrow 5d$ transitions, a single DF calculation predicts a much wider absorption band than a CI calculation around a photon energy of 80 eV. In other words, the CI effect results in a strong narrowing absorption for these strong lines. For example, the strongest absorption located near 79 eV in Fig. 3(b) is contributed by two fine-structure lines $5d_{5/2} \rightarrow ((5p_{1/2}^{-1}5d_{3/2})_15d_{5/2})_{7/2}$ (79.11 eV) and

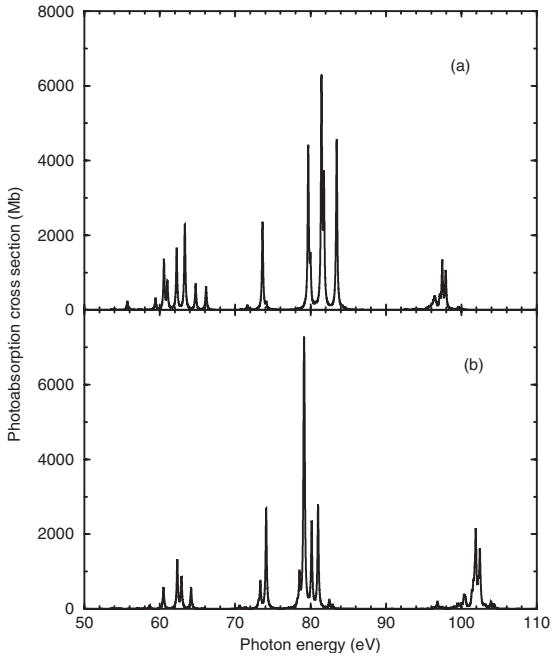

FIG. 3. Absorption cross section caused by transition arrays of $4f^{14}5p^65d \rightarrow 4f^{14}5p^55d^2$ and $4f^{14}5p^65d \rightarrow 4f^{13}5p^65d^2$ of Au^{10+} obtained by using (a) a single-configuration DF calculation and (b) a full CI calculation.

$5d_{5/2} \rightarrow ((5p_{3/2}^{-1}5d_{3/2})_1 5d_{5/2})_{5/2}$ (79.18 eV). These two lines are so closely located that they look like one individual line. Such a narrowing phenomenon is particularly evident for more complex transition arrays such as $4f^{14}5p^55d^2 \rightarrow 4f^{14}5p^45d^3$ and $4f^{13}5p^65d^2 \rightarrow 4f^{13}5p^55d^3$. On the whole, the CI effect results in a net transfer of oscillator strengths from the transition array of $4f^{14}5p^65d \rightarrow 4f^{14}5p^55d^2$ to $4f^{14}5p^65d \rightarrow 4f^{13}5p^65d^2$. Moreover, the CI effect changes line position, resulting in a shift toward lower photon energy for $5p \rightarrow 5d$ transitions and a shift toward higher energy for lines of $4f \rightarrow 5d$. The redistribution of gf values between a transition array, or even between different arrays will certainly have large effects on the radiative opacity. To have a quantitative understanding, Table I gives the weighted oscillator strengths for some strong transitions of the two transition arrays.

For the bound-free (photoionization) process, the physical effects affecting the bound-bound process also influence the accuracy of the photoionization cross section. In addition, the effect of continuous free electrons should be taken into account as well. One simple treatment of this kind of process is to calculate the cross section for every level of every configuration needed in opacity calculations one by one by using a distorted-wave approximation [29]. Each configuration in a given ionization stage is connected to various configurations in the next higher one, corresponding to removing one electron in different shells. For example, the cross section for levels of the configuration $4s^24p^64d^{10}4f^{14}5s^25p^6$ of Au^{11+} include

TABLE I. Weighted oscillator strengths (with $gf > 1$) and transition energies ΔE (in eV) of Au^{10+} for transition arrays $4f^{14}5p^65d \rightarrow 4f^{14}5p^55d^2$ and $4f^{14}5p^65d \rightarrow 4f^{13}5p^65d^2$ obtained by using full electron correlations. Full relativistic subshells have been omitted for the designation of levels.

Lower	Upper level	Upper J	ΔE	gf
$5d_{3/2}$	$(5p_{3/2}^{-1}5d_{3/2})_3 5d_{5/2}$	3/2	60.49	1.425
$5d_{3/2}$	$(5p_{3/2}^{-1}5d_{3/2})_3 5d_{5/2}$	1/2	64.15	1.418
$5d_{3/2}$	$(5p_{1/2}^{-1}5d_{3/2})_2 5d_{5/2}$	5/2	73.34	1.772
$5d_{3/2}$	$5p_{1/2}^{-1}(5d_{3/2}^2)_2$	5/2	74.11	6.748
$5d_{3/2}$	$5p_{1/2}^{-1}(5d_{3/2}^2)_0$	1/2	78.53	2.119
$5d_{3/2}$	$5p_{1/2}^{-1}(5d_{3/2}^2)_2$	3/2	80.99	6.948
$5d_{3/2}$	$4f_{7/2}^{-1}(5d_{5/2}^2)_2$	3/2	101.76	1.071
$5d_{3/2}$	$4f_{7/2}^{-1}(5d_{5/2}^2)_2$	5/2	102.23	1.198
$5d_{5/2}$	$5p_{3/2}^{-1}(5d_{5/2}^2)_4$	5/2	62.32	3.281
$5d_{5/2}$	$5p_{3/2}^{-1}(5d_{5/2}^2)_2$	3/2	62.88	2.122
$5d_{5/2}$	$(5p_{1/2}^{-1}5d_{3/2})_1 5d_{5/2}$	7/2	79.11	11.208
$5d_{5/2}$	$(5p_{3/2}^{-1}5d_{3/2})_1 5d_{5/2}$	5/2	79.18	9.865
$5d_{5/2}$	$(5p_{3/2}^{-1}5d_{3/2})_1 5d_{5/2}$	3/2	80.14	5.687
$5d_{5/2}$	$(4f_{5/2}^{-1}5d_{3/2})_1 5d_{5/2}$	3/2	101.59	1.114
$5d_{5/2}$	$(5p_{3/2}^{-1}5d_{3/2})_1 5d_{5/2}$	7/2	101.90	4.181
$5d_{5/2}$	$(5p_{3/2}^{-1}5d_{3/2})_1 5d_{5/2}$	5/2	102.45	3.139

$$
\begin{aligned}
4s^24p^64d^{10}4f^{14}5s^25p^6 &\rightarrow 4s^24p^64d^{10}4f^{14}5s^25p^5 + e^- \\
&\rightarrow 4s^24p^64d^{10}4f^{14}5s5p^6 + e^- \\
&\rightarrow 4s^24p^64d^{10}4f^{13}5s^25p^6 + e^- \\
&\rightarrow 4s^24p^64d^94f^{14}5s^25p^6 + e^- \\
&\rightarrow 4s^24p^54d^{10}4f^{14}5s^25p^6 + e^- \\
&\rightarrow 4s4p^64d^{10}4f^{14}5s^25p^6 + e^-.
\end{aligned}
$$

The core $1s^22s^22p^63s^23p^63d^{10}$ is fixed, and therefore contributions from these inner-shell orbitals $1s$, $2s$, $2p$, $3s$, $3p$, and $3d$ are not taken into account in photoionization cross sections. The fine-structure level effects and interaction of intraconfigurations are included in the photoionization cross section.

A more complete and accurate treatment of the bound-free process, however, should include the CI effect both for initial and final states. As a result, the treatment of the CI effect is even more complicated than the bound-bound process. We take a similar scale of the CI effect as for the bound-bound process to obtain the photoionization cross section. For those configurations with energetically lower electronic orbitals, we use a large-scale CI calculation, while for configurations of more highly excited orbitals, we use a single-configuration approximation to obtain the photoionization cross section. In order to take more electron correlations into account, photoionization processes from electron shells of $4s$, $4p$, and $4d$ have not been included in the large-scale CI calculation because the interactions from these configurations are small compared with the excitation of $5p$ and $4f$ electrons. Their contributions to the photoionization cross section are ob-

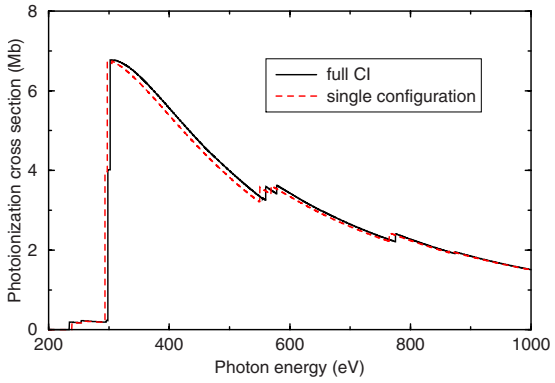

FIG. 4. (Color online) Photoionization cross section from the ground level of Au^{11+}. The solid and dashed lines refer to results with and without the CI effect being considered.

tained by separate calculations. In such a way, the main electron correlations can be taken into account and cross sections can be obtained relatively faster and easier while maintaining computational accuracy.

Figure 4 shows the photoionization cross section of the ground level $(5p^6)_0$ of Au^{11+} by using the two methods described above. The solid and dashed lines refer to results of large-scale CI and single-configuration DF calculations, respectively. In principle, atomic data including the oscillator strength and photoionization cross section are influenced by the plasma environment. However, for the plasma temperature and density presented in this work, the effects of such a plasma environment should be very small. Saha and Fritzsche [31] investigated the influence of a dense plasma on the low-lying transitions in Be-like ions. Their results showed that with an increase of the atomic number, this effect is negligibly small even at an electron density of 1.0×10^{25} for Mo^{38+} (Z=42). For Au plasmas, the effect of the plasma environment at the same electron density should be even smaller.

From inspection of Fig. 4, one can find that the two results obtained by different methods are fairly close except for a slight enhancement of the $4f$ ionization cross section and a slight difference of the ionization thresholds. The first small rise of the cross section is due to the opening of the $5p$ ionization channel; then, the rapid increase near 300 eV is contributed by $4f$. The structures near 560 and 770 eV are due to the opening of $4d$ and $4p$ ionization channels, while the contribution of $4s$ near 870 eV is nearly invisible. The relativistic splitting of photoionization originating from the orbitals $4f_{5/2}$, $4f_{7/2}$, $4d_{3/2}$, $4d_{5/2}$, $4p_{1/2}$, and $4p_{3/2}$ is clearly seen in the figure. Among all these relativistic orbitals, the splitting of the $4d$ channel is the largest. Practical calculations show that the CI effect has a more evident contribution for more complex configurations. To have a more complete view of the bound-free process, we show in Fig. 5 photoionization cross sections from 12 levels of the first excited configuration $5p^55d$: $(5p_{3/2}5d_{3/2})_{0,1,3,2}$ [(a), (b), (c), (d)], $(5p_{3/2}5d_{5/2})_{4,2,3,1}$ [(e), (f), (g), (h)], $(5p_{1/2}5d_{3/2})_2$ [(i)], $(5p_{1/2}5d_{5/2})_{2,3}$ [(j), (k)], and $(5p_{1/2}5d_{3/2})_1$ [(l)]. The cross sections have been added successively by 1 MB except for levels (a) and (g). The configuration $5p^55d$ has full $4f$, $4d$, and

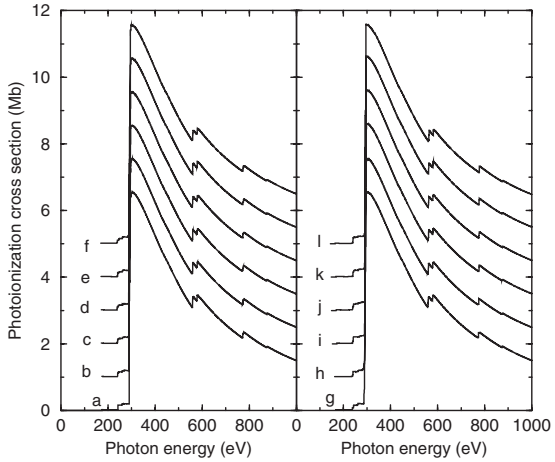

FIG. 5. Photoionization cross sections from 12 levels of first excited configuration $5p^55d$ of Au^{11+}. See text for detailed level designation.

$4p$ subshells, and therefore their contributions to the cross sections of all 12 levels are basically the same. The largest difference is near the thresholds, which is due entirely to the different angular coupling schemes.

C. Opacity

Once all the atomic data required have been obtained, it is a easy step to obtain the radiative opacity. Figure 6(a) shows the opacity contributed by bound-bound (solid line) and bound-free (dashed line) absorptions, and Fig. 6(b) shows

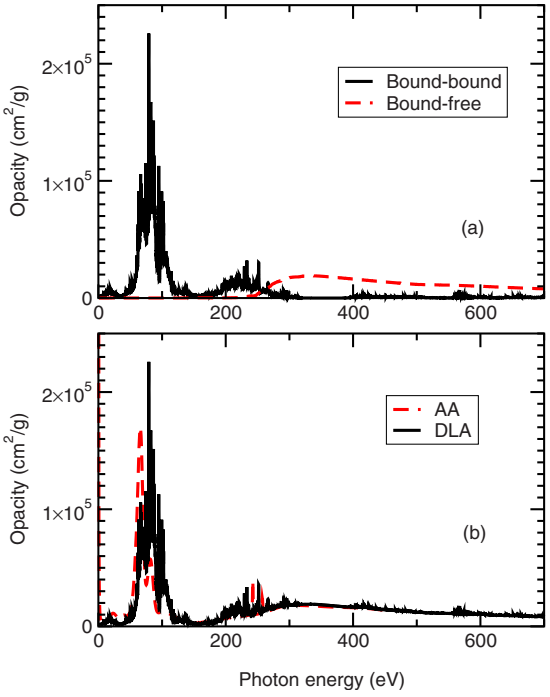

FIG. 6. (Color online) (a) Bound-bound and bound-free opacities and (b) total opacity at a temperature of 22.5 eV and a density of 0.007 g/cm^3.

TABLE II. Rosseland and Planck mean opacities for Au plasmas obtained by the DLA and AA approaches.

Physical condition	DLA Rosseland	DLA Planck	AA Rosseland	AA Planck
22.5 eV, 0.007 g/cm^3	5928	27607	9784	29314
22 eV, 0.005 g/cm^3	6301	28139	9786	29621
23.6 eV, 0.01 g/cm^3	6502	27121	9635	28078
27.5 eV, 0.05 g/cm^3	7336	24868	9065	24603
29.2 eV, 0.1 g/cm^3	7400	22945	8842	23313

the total opacity, in which the CI effect has been included. For comparison, the result obtained by the AA model is also shown. It can be seen that below a photon energy of 250 eV, bound-bound absorption dominates the opacity, while above 250 eV, bound-free absorption does. The strongest absorption located near 80 eV originates from $5s$-$5p$ and $5p$-$5d$ transitions, while structures near 100 eV are mainly contributed by $4f$-$5d$ transitions. This is consistent with our analyses discussed above. At higher photon energy (above 400 eV), there are some small structures which are caused by excitation of $4d$ and $4p$ subshells. However, their contribution to the opacity is trivial compared with that of the bound-free process in this energy region. Therefore, electrons in subshells of $4d$ and $4p$ manifest their contributions to opacity dominantly through bound-free process, not through the bound-bound ones. This is different from the case of the $4f$ subshell, which has both evident bound-bound and bound-free opacities. For instance, the structures near 100 eV originate from $4f$-$5d$ bound-bound transitions and the structures around 210 eV from $4f$-ng, nd transitions, while the continuum opacity near 300 eV is primarily due to the $4f$ photoionization channel. At lower photon energy, opacity is mainly contributed by bound-bound absorption. The bound-free opacity is due solely to the photoionization of the valence electrons and therefore their contribution is negligibly small.

From inspection of Fig. 6(b), one can see that rather good agreement is found between DLA and AA opacity above 200 eV, especially for bound-free absorption. At an energy of above 300 eV, the opacity obtained by the DLA and AA models is nearly the same. Such good agreement between the two different treatments showed that the treatment of bound-free opacity should be valid and correct. In the lower-energy region, however, the opacity is dominated by bound-bound absorption structures. The DLA approach predicts all fine structures of opacity, while the AA model only predicts a gross profile. The position of the strongest absorption peak predicted by the AA model is much lower than that by the DLA method. The structures of strong absorption peaks around 80 eV are mainly contributed by $5s$-$5p$, $5p$-$5d$, and $4f$-$5d$ transitions. The strongest one is due to $5p$-$5d$ transitions, the next strongest one to $5s$-$5p$. However, $5p$-$5d$ transitions have a contribution in the $5s$-$5p$ peak as well. If one does not include adequate CIs, then one predicts much stronger absorption in the energy region of the $5s$-$5p$ peak, which can be seen from Fig. 3. Because of the same reason, the AA model predicts a much stronger absorption for $5s$-$5p$ than for $5p$-$5d$, which is in disagreement with experiment. The detailed difference between the two methods will result in a discrepancy between the Rosseland and Planck means, in particular for the Rosseland mean opacity. Table II lists the Rosseland and Planck means obtained by the DLA and AA approaches. For Au plasma at the temperature of 22.5 eV and density of 0.007 g/cm^3, the DLA scheme predicts a Rosseland mean of 27 607 cm^2/g, which is rather close to the AA result of 29 314 cm^2/g. For the Rosseland mean, however, a relatively large difference is found. The difference relative to the DLA Rosseland mean is about 60%. As mentioned above, the difference between the two methods may due more heavily to the relevant physical effects on the opacity than the theoretical method itself. If an adequate CI effect can be considered in statistical models such as AA, then they may predict a similar overall profile of absorption to the DLA method. Actually, if the CI effect is not fully considered in bound-bound absorption, then the DLA formalism predicts the Planck mean opacity to be 29 340 cm^2/g, which is nearly equal to that of the AA result 29 314 cm^2/g. While the Rosseland mean opacity is 4336 cm^2/g, which is smaller than the DLA treatment, which takes the complete CI effect into account, though the former method predicts much stronger absorption.

Physical effects such as the CI and linewidth on the radiative opacity have been demonstrated in our previous work [11]. From the comparison of Figs. 1 and 2 in that work [11], one can see that our DLA results agree much better with experiment after the main physical effects have been considered. The result correctly explains the relative intensity of the strong absorption peaks due to $5s$-$5p$ and $5p$-$5d$ transitions.

D. Sequence of isoionization degree 10

Using the same procedure, we investigated the radiative opacity of Au plasmas with different physical conditions

TABLE III. Population fraction (%) of the dominant charge-state distribution, average ionization degree of Au plasmas under different physical condition.

Physical condition	Au^{7+}	Au^{8+}	Au^{9+}	Au^{10+}	Au^{11+}	Au^{12+}	Au^{13+}	Z^*
22.5 eV, 0.007 g/cm^3	0.7	7.6	30.8	34.4	16.2	9.8	0.4	9.89
22 eV, 0.005 g/cm^3	0.5	6.2	28.6	35.4	17.8	11.0	0.5	10.0
23.6 eV, 0.01 g/cm^3	0.7	6.8	27.8	33.0	17.6	13.3	0.7	10.0
27.5 eV, 0.05 g/cm^3	1.3	9.0	27.7	28.1	15.5	16.7	1.5	10.0
29.2 eV, 0.1 g/cm^3	1.8	10.1	28.0	26.3	14.3	17.3	1.9	10.0

TABLE IV. Partition functions of Au ions under different plasma physical conditions.

Ionization stage	22.5 eV 0.007 g/cm^3	22 eV 0.005 g/cm^3	23.6 eV 0.01 g/cm^3	27.5 eV 0.05 g/cm^3	29.2 eV 0.1 g/cm^3
Au^{0+}	4043	4045	4100	3786	3223
Au^{1+}	3930	4256	3888	1938	958
Au^{2+}	9024	9178	8398	4478	2659
Au^{3+}	8117	8232	7565	4938	3736
Au^{4+}	8128	8266	8357	6559	5280
Au^{5+}	5652	5543	6065	5732	4986
Au^{6+}	3468	3370	3758	3909	3680
Au^{7+}	1691	1626	1926	2181	2128
Au^{8+}	694	654	794	1018	1028
Au^{9+}	239	223	276	396	431
Au^{10+}	51.7	47.9	60.8	96.5	110.9
Au^{11+}	10.3	9.4	12.7	23.5	28.8
Au^{12+}	29.2	26.3	36.7	77.3	101.6
Au^{13+}	41.3	37.6	51.0	105.3	138.5
Au^{14+}	42.0	38.3	51.6	105.6	140.9

along an isoionization degree sequence at temperatures and densities of 22 eV and 0.005 g/cm^3, 23.6 eV and 0.01 g/cm^3, 27.5 eV and 0.05 g/cm^3, and 29.2 eV and 0.1 g/cm^3, respectively. The average ionization degree Z^* is 10 for all four cases. Under these physical conditions, the fraction of dominant ion types in the plasma is given in Table III. With an increase of mass density, the maximal fraction of dominant ion types decrease and redistribute the population over wider ionization stages, and the magnitude of the relative abundance of Au^{11+} and Au^{12+} is reversed compared to a low density. At a density of 0.05 g/cm^3, the fractions of these two ions are 15.5% and 16.7%, respectively, which is only slightly reversed, while they are 14.3% and 17.3%, respectively, at a density of 0.1 g/cm^3. Such a variational trend is a combined effect of the ionization potential and partition function of respective ions on the ionization equilibrium equation. Being helpful to understand such a conclusion, we list partition functions of various Au ions in Table IV. For Au^{11+}, it has a closed-shell structure $5s^25p^6$ and therefore has a higher ionization potential. At low densities, the ionization potential plays a more important role to determine the relative abundance. However, with an increase of the density—i.e., an increase of temperature—the effects of the ionization potential and partition function compete and then the role of the partition function slowly dominates over that of the ionization potential for Au^{11+} and Au^{12+}. The main reason is due to the strong sensitivity of the partition function to temperature. For example, the partition functions are 9.4 and 26.3 for Au^{11+} and Au^{12+}, respectively, at 0.005 g/cm^3 (temperature of 22 eV), while they are 28.8 and 101.6, respectively, at 0.1 g/cm^3 (temperature of 29.2 eV). For lower ionization stages such as Au^{8+}-Au^{10+}, the increase of partition functions with temperature shows less significance compared with those of Au^{11+} and Au^{12+}. As a result, the partition function of Au^{12+} increases faster than Au^{11+} with temperature, but the ionization potential does not change much, resulting in an abundance inversion between Au^{11+} and Au^{12+} ions.

The spectrally resolved radiative opacity for $Z^* \sim 10$ sequence is shown in Fig. 7, with the solid and dashed lines referring to the DLA and AA results, respectively. Note that

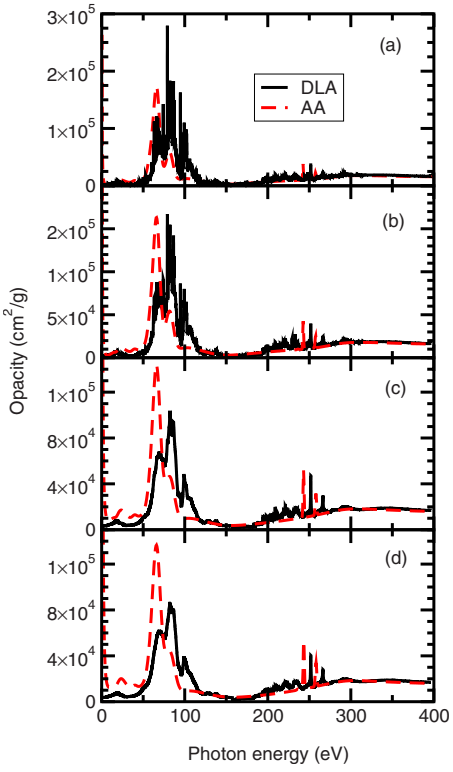

FIG. 7. (Color online) Spectrally resolved radiative opacity for the $Z^* \sim 10$ sequence: (a) 22 eV and 0.005 g/cm^3, (b) 23.6 eV and 0.01 g/cm^3, (c) 27.5 eV and 0.05 g/cm^3, and (d) 29.2 eV and 0.1 g/cm^3. The solid and dashed lines refer to the DLA and AA results, respectively.

the different scale of the opacity axis is used to have an optimal illustration of the results. As can be seen, the linewidth is very small at a density of 0.005 g/cm^3. With an increase of the density, the linewidth becomes larger and larger and detailed absorption structures merge together. The increase of the linewidth with density is due to the electron impact broadening mechanism. However, the overall background of the strongest absorption peaks around 80 eV is basically the same ($\sim$50 000 cm^2/g), resulting in a slow increase with density for the Rosseland mean (see Table II). The main reason is that so many individual lines coalesce to form a quasicontinuum broad absorption band that the width of individual lines does not play so important a role in the Rosseland mean. This is not to say that the role of individual linewidths is unimportant, but to say that some certain inaccuracy in the linewidth for a given plasma density does not influence the opacity considerably. For a different plasma density, the effect of the linewidth can be easily seen from the variational trend from Fig. 7(a) to Fig. 7(d). Actually, the complex atomic structures of high-Z ions are the direct reason for so many lines involved in absorption. Such a role of the individual linewidth of the Rosseland mean is much less important than in aluminium plasmas [32]. For aluminum plasmas, the Rosseland mean is very sensitive to the density for the $Z^* \sim 7.13$ sequence. With density increasing from 0.001 g/cm^3 to 0.1 g/cm^3, the Rosseland mean increases a factor of 9. The Planck mean, however, decreases with density, also unlike aluminum plasmas [32], which increase with density.

The AA model predicts the strongest absorption at a much lower energy than the DLA model does. At a density of 0.005 g/cm^3, the absorption shows two peaks. With an increase of density, the two peaks slowly merge together. The peak at a lower energy is much stronger than the peak at higher energy, which is due to neglect of the CI effect. Although a large difference is found between the DLA and AA spectrally resolved opacity, there is not so large a difference for the mean opacities. The Planck means agree very well with each other, the relative difference being within 5%, while the relative difference reaches 60% for the Rosseland mean between DLA and AA results. Such a conclusion is dramatically different from aluminum plasmas [32], for which the Rosseland mean can differ by a factor of 9 between DTA and AA models.

E. Summary

In conclusion, spectrally resolved opacities and Rosseland and Planck means of Au plasmas under a variety of physical condition have been investigated in detail by using a DLA method. A fine treatment for every individual line by considering physical effects such as relativity, core-valence electron correlation, and autoionization width is essential to correctly reproduce the fine structures of the radiative opacity of gold plasmas, although there are so many individual lines that statistical models can often give reasonable simulations for general characteristics. In this work, as an example of statistical models we use the AA model to illustrate the general characteristics of opacities of Au plasmas. Practical calculations showed that DLA scheme can give detailed information including the fine-structure absorptions, while AA model can only give an overall smoothed absorption profile on opacity. The present work showed that the DLA approach is feasible and helpful to resolve discrepancies between theory and experiment for high-Z material such as Au plasmas, although a lot of computational effort is needed to obtain accurate opacity.

In this work, we obtained Rosseland and Planck mean opacities at a given temperature and density in about 5 computer hours using the AA model. To obtain the atomic data required for DLA calculations, we spent about 12 000 computer hours. Therefore we developed a simple parallel code to generate the required atomic data. However, once these data have been obtained, they can be stored and used in the future.

ACKNOWLEDGMENTS

This work was supported by the Program for New Century Excellent Talents in University (NCET) and the National Natural Science Foundation of China under Grants No. 10474138 and No. 10604067.

[1] E. Storm, J. Fusion Energy **7**, 131 (1988); R. L. Kauffman *et al.*, Phys. Rev. Lett. **73**, 2320 (1994).
[2] F. J. Rogers and C. A. Iglesias, Science **263**, 50 (1994); C. A. Iglesias *et al.*, Astrophys. J. **445**, 855 (1995).
[3] T. S. Perry *et al.*, Phys. Rev. Lett. **67**, 3784 (1991).
[4] Jiaolong Zeng, Fengtao Jin, Jianmin Yuan, Qisheng Lu, and Yongsheng Sun, Phys. Rev. E **62**, 7251 (2000).
[5] C. A. Iglesias, J. K. Nash, M. H. Chen, and F. J. Rogers, J. Quant. Spectrosc. Radiat. Transf. **51**, 125 (1994).
[6] J. Abdallah and R. E. H. Clark, J. Appl. Phys. **69**, 23 (1991).
[7] T. S. Perry *et al.*, J. Quant. Spectrosc. Radiat. Transf. **54**, 317 (1995).
[8] K. Eidmann, A. Bar-Shalom, A. Saemann, and G. Winhart, Europhys. Lett. **44**, 459 (1998).
[9] C. A. Iglesias *et al.*, J. Quant. Spectrosc. Radiat. Transf. **81**, 227 (2003).
[10] C. A. Iglesias, J. Quant. Spectrosc. Radiat. Transf. **99**, 295 (2006).
[11] Jiaolong Zeng and Jianmin Yuan, Phys. Rev. E **74**, 025401(R) (2006).
[12] O. S. Jones *et al.*, Phys. Rev. Lett. **93**, 065002 (2004).
[13] E. L. Dewald *et al.*, Phys. Rev. Lett. **95**, 215004 (2005).
[14] J. Yan and Z. Q. Wu, Phys. Rev. E **65**, 066401 (2002).
[15] C. Bauche-Arnoult, J. Bauche, and M. Klapisch, J. Opt. Soc. Am. **68**, 1136 (1978).
[16] C. Bauche-Arnoult, J. Bauche, and M. Klapisch, Adv. At. Mol. Phys. **23**, 131 (1987).
[17] A. Bar-Shalom, J. Oreg, W. H. Goldstein, D. Shvarts, and A.

Zigler, Phys. Rev. A **40**, 3183 (1989).
[18] Y. S. Sun, X. J. Meng, and S. T. Zheng, Nucl. Sci. Techniques **8**, 6 (1997).
[19] Jianmin Yuan, Phys. Rev. E **66**, 047401 (2002).
[20] Jianmin Yuan, Chin. Phys. Lett. **19**, 1459 (2002).
[21] Jinqiao Pang, Zeqing Wu, Jun Yan, and Guoxing Han, Chin. Phys. Lett. **21**, 2005 (2004).
[22] Zeqing Wu, Jinqiao Pang, and Jun Yan, J. Quant. Spectrosc. Radiat. Transf. **102**, 402 (2006).
[23] Rodolphe Turpault, J. Quant. Spectrosc. Radiat. Transf. **94**, 357 (2005).
[24] Jiaolong Zeng, Jianmin Yuan, and Qisheng Lu, Phys. Rev. E **64**, 066412 (2001).
[25] Jiaolong Zeng, Gang Zhao, and Jianmin Yuan, Phys. Rev. E **70**, 027401 (2004).
[26] Fengtao Jin and Jianmin Yuan, Phys. Rev. E **72**, 016404 (2005).
[27] R. D. Cowan, *Theory of Atomic Spectra* (University of California Press, Berkeley, 1981).
[28] D. J. Heading, J. S. Wark, G. R. Bennett, and R. W. Lee, J. Quant. Spectrosc. Radiat. Transf. **54**, 167 (1995), and references therein.
[29] M. F. Gu, Astrophys. J. **582**, 1241 (2003).
[30] Jiaolong Zeng, Gang Zhao, and Jianmin Yuan, J. Quant. Spectrosc. Radiat. Transf. **102**, 172 (2006).
[31] B. Saha and S. Fritzsche, J. Phys. B **40**, 259 (2007).
[32] Jiaolong Zeng and Jianmin Yuan, Phys. Rev. E **66**, 016401 (2002).